Table 2 Summary of typical reversible model without arterial input function

Estimated physiological parameter	SRTM	SRTM2	LGA	MRTM0	MRTM	MRTM2
	$R_1, k_2,$ BP	$R_1,$ BP	V_R	V_R, k_2'	V_R, k_2'	V_R
k_2'	Variable	Fixed	Fixed	Variable	Variable	Fixed
Fitting range	0, End frame	0, End frame	$t > t^*$	$t > t^*$	$t > t^*$	$t > t^*$
Fitting algorithm	Nonlinear / Basis function	Nonlinear / Basis function	Linear	Multilinear	Multilinear	Multilinear
Estimation speed	Slow / Fast	Slow / Fast	Fast	Fast	Fast	Fast
Estimation error	Bias is small; COV is large in a high noise level or low BP; There are no outliers	Bias is small; COV is small	Bias is large; COV is small	Bias is large; COV is small	Bias of MRTM0 is eliminated; COV is large	Bias of LGA is eliminated; COV is small

SRTM simplified reference tissue model, *LGA* Logan graphical analysis, *MRTM* multilinear reference tissue model, t^* equilibrium time

parameter irreversible model is sufficient to describe the tissue TAC when scan duration is less than 60 min [35, 36]. An irreversible model is also utilized for quantification of metabolism with other tracers, such as presynaptic dopaminergic function with [18F]FDOPA [37–39].

Compartmental analysis

The solution of the irreversible model is expressed as Eq. 11, and CMRGlc is calculated from Eq. 12 [34, 40]:

$$C_t(t) = \frac{K_1}{k_2+k_3}(k_3 + k_2 e^{-(k_2+k_3)t}) \otimes C_p(t) \tag{11}$$

$$CMPGlc = \frac{1}{LC}\frac{K_1 k_3}{k_2+k_3}C_p^* \tag{12}$$

where C_p^* is the capillary plasma glucose concentration and LC is the lumped constant that accounts for differences in transport and phosphorylation between FDG and glucose. Each parameter is estimated by NLS in the same way as for the reversible compartment model. There is little bias at a low noise level, while the COV is larger than graphical analysis. The fitting procedure is iterative, and so it is computationally expensive.

Several methods with LLS, such as weighted integration method (WIM) [12, 41] and LLS method that is similar to the reversible model [42]. In these methods, parameters are estimated by linear regression, and therefore, the processing speed is fast. However, the bias is larger than with NLS especially at a high noise level, and COV is the same level or larger than NLS [12]. Generalized linear least-squares method (GLLS), which solves the problem of biased estimates in LLS, was also established; however, the COV is not small.

Reducing the estimation error of these compartmental analysis methods has been approached by denoising the TAC before parameter estimation with cluster analysis or wavelet transform [43, 44].

Graphical analysis

On the other hand, the graphical analysis of Patlak (PGA) was developed [45] as follows:

$$\frac{C_t(T)}{C_p(T)} = K_i \frac{\int_0^T C_p(t)dt}{C_p(T)} + \frac{K_1 k_2}{(k_2+k_3)^2} \quad \text{for} \quad t > t^* \tag{13}$$

$K_i = K_1 k_3/(k_2 + k_3)$ can be obtained by fitting the slope of the line after equilibrium t^*, i.e., $dC_f/dt = 0$, where C_f is the radioactivity concentration of nonmetabolized tracer in the tissue. Advantages of PGA are its computational

efficiency and stability of estimates, and disadvantages are that the individual rate constants are not estimated and the K_i value is often underestimated even with a low noise level if the value of k_4 cannot be ignored [12]. Lack of equilibration is of greatest relevance at early times whereas loss of metabolic product is most relevant at later times. Therefore, the most appropriate time interval should be chosen according to the tracer and target tissue [46, 47]. Noise-induced bias observed in LGA does not appear in PGA because $C_i(t)$ with PET measurement noise is not included in the right side of Eq. 13.

Feng et al. [12] compared the uncertainty of these methods, NLS, LLS, WIM, GLLS, and PGA by a computer simulation with K_1-k_4 for 120-min scan of FDG, reporting that the K_i value by PGA was underestimated and that by WIM was overestimated even at a low noise level, and that there was little bias in NLS and LLS although underestimation was observed at a high noise level. COV of PGA was smaller than one-fifth in other methods, and that of LLS was largest.

Bootstrap approach for error estimation in human data

As mentioned above, the relationship between reliability and noise level of the target TAC was investigated in a simulation study. However, estimating the reliability of human data is not easy because the noise model from human data is complex and the true noise level is not precisely known. Moreover, the noise level varied according to not only camera sensitivity but also the kinetics of the individual, injection dosage, ROI size, and so on. Thereafter, the noise level of human data was deduced from the residual error of least-squares fitting by comparing them with those in the simulation [29, 48], or from SD of the reconstructed images of a phantom study [49].

To overcome the above limitations, a computer-based statistical approach, the so-called bootstrap approach has been often applied to dynamic PET data [50–53]. The bootstrap approach facilitates estimation of the variability of the statistic of interest by estimating uncertainly, e.g., average or SD of many replicated samples generated not from repeated measurements but from random resampling of measured data without specifying their distribution on the assumptions about errors such as independence, identical distribution, and zero mean [54]. For example, in compartmental analysis, the uncertainty of kinetic parameters estimated from an ROI or voxel TAC was evaluated from many replicated TACs generated by resampling weighted residual errors between measured and model-predicted TAC [50–53]. On the other hand, reconstructed radioactivity images

are replicated by resampling sub-sinograms obtained with list-mode or gated acquisition [55], and it would be possible to apply not only for methods involving least-squares fitting of TAC with compartmental models but also for other methods. The bootstrap approach is one method for error estimation in PET kinetic analysis, and is useful because it can be done from the measured data without the need to specify the distribution of noise in PET measurement.

Conclusions

Many methods have been developed to quantify the biomedical functions from PET data. There are both advantages and disadvantages to each method, and the influence of noise varies. A compartmental analysis with NLS provides kinetic parameters such as K_1-k_4 and is free from biases, which originated in linearization or simplification. However, estimated parameters are sensitive to the noise and the fitting procedure is computationally very expensive. Conversely, graphical analysis of Logan is simple, stable, and the estimation process is rapid. However, this method can yield only V_T and causes a noise-induced bias. We must choose the optimal analysis method according to the tracer properties and ends, for example, whether the kinetics are fast or slow, whether the reference region can be determined, what a required function parameter is, how much the noise level of the targeted tissue TAC is, and whether it is an ROI-based estimation or voxel-based estimation.

References

1. Kety SS. The theory and applications of the exchange of inert gas at the lungs and tissues. Pharmacol Rev 1951;3:1–41.
2. Reivich M, Kuhl D, Wolf A, Greenberg J, Phelps M, Ido T, et al. The [18F]fluorodeoxyglucose method for the measurement of local cerebral glucose utilization in man. Circ Res 1979;44:127–37.
3. Mintun MA, Raichle ME, Kilbourn MR, Wooten GF, Welch MJ. A quantitative model for the in vivo assessment of drug binding sites with positron emission tomography. Ann Neurol 1984;15:217–27.
4. Watabe H, Ikoma Y, Kimura Y, Naganawa M, Shidahara M. PET kinetic analysis: compartmental model. Ann Nucl Med 2006;20:583–8.
5. Koeppe RA, Holthoff VA, Frey KA, Kilbourn MR, Kuhl DE. Compartmental analysis of [11C]flumazenil kinetics for the estimation of ligand transport rate and receptor distribution using positron emission tomography. J Cereb Blood Flow Metab 1991;11:735–44.
6. Press WH, Flannery BP, Teukolsky SA, Vetterling WT. Numerical recipes in C. Cambridge: Cambridge University Press; 1988.
7. Luenberger DG. Optimization by vector space methods. New York: Wiley; 1969. p. 271–311.

8. Marquardt DW. An algorithm for least squares estimation of nonlinear parameters. SIAM J Soc Ind Appl Math 1963;2: 431–41.

9. Ikoma Y, Yasuno F, Ito H, Suhara T, Ota M, Toyama H, et al. Quantitative analysis for estimating binding potential of the peripheral benzodiazepine receptor with [¹¹C]DAA1106. J Cereb Blood Flow Metab 2007;27:173–84.

10. Ikoma Y, Takano A, Ito H, Kusuhara H, Sugiyama Y, Arakawa R, et al. Quantitative analysis of ¹¹C-Verapamil transfer at the human blood–brain barrier for evaluation of P-glucoprotein function. J Nucl Med 2006;47:1531–7.

11. Ikoma Y, Toyama H, Yamada T, Uemura K, Kimura Y, Senda M, et al. Creation of a dynamic digital phantom and its application to a kinetic analysis. Kaku Igaku 1998;35: 293–303.

12. Feng D, Ho D, Chen K, Wu LC, Wang JK, Liu RS, et al. An evaluation of the algorithms for determining local cerebral metabolic rates of glucose using positron emission tomography dynamic data. IEEE Trans Med Imaging 1995;14: 697–710.

13. Ichise M, Toyama H, Innis RB, Carson RE. Strategies to improve neuroreceptor parameter estimation by linear regression analysis. J Cereb Blood Flow Metab 2002;22:1271–81.

14. Logan J, Fowler JS, Volkow ND, Wolf AP, Dewey SL, Schlyer DJ, et al. Graphical analysis of reversible radioligand binding from time–activity measurements applied to [N-11C-methyl]-(–)-cocaine PET studies in human subjects. J Cereb Blood Flow Metab 1990;10:740–7.

15. Kimura Y, Naganawa M, Shidahara M, Ikoma Y, Watabe H. PET kinetic analysis: pitfall and solution for Logan plot. Ann Nucl Med 2007;21:1–8.

16. Slifstein M, Laruelle M. Effects of statistical noise on graphic analysis of PET neuroreceptor studies. J Nucl Med 2000;41: 2083–8.

17. Logan J, Fowler JS, Volkow ND, Ding YS, Wang GJ, Alexoff DL. A strategy for removing the bias in the graphical analysis method. J Cereb Blood Flow Metab 2001;21:307–20.

18. Varga J, Szabo Z. Modified regression model for the Logan plot. J Cereb Blood Flow Metab 2002;22:240–4.

19. Carson RE. PET parameter estimation using linear integration methods: bias and variability consideration. In: Uemura K, Lassen NA, Jones T, Kanno I, editors. Quantification of brain function: tracer kinetics and image analysis in brain PET. Amsterdam: Elsevier Science; 1993. p. 499–507.

20. Ogden RT. Estimation of kinetic parameter in graphical analysis of PET imaging data. Stat Med 2003;22:2557–68.

21. Burger C, Buck A. Requirements and implementation of a flexible kinetic modeling tool. J Nucl Med 1997;38:1818–23.

22. Olsson H, Halldin C, Swahn CG, Fardc L. Quantification of [¹¹C]FLB457 binding to extrastriatal dopamine receptors in the human brain. J Cereb Blood Flow Metab 1999;19: 1164–73.

23. Carson RE, Yan Y, Daube-Witherspoon ME, Freedman N, Bacharach SL, Herscovitch. An approximation formula for the variance of PET region-of-interest values. IEEE Trans Med Imaging 1993;12:240–50.

24. Lammertsma AA, Hume SP. Simplified reference tissue model for PET receptor studies. Neuroimage 1996;4:153–8.

25. Logan J, Fowler JS, Volkow ND, Wang GJ, Ding YS, Alexoff DL. Distribution volume ratios without blood sampling from graphical analysis of PET data. J Cereb Blood Flow Metab 1996;16:834–40.

26. Hume SP, Myers R, Bloomfield PM, Opacka-Juffry J, Cremer JE, Ahier RG, et al. Quantitation of carbon-11-labeled raclopride in rat striatum using positron emission tomography. Synapse 1992;12:47–54.

27. Lammertsma AA, Bench CJ, Hume SP, Osman S, Gunn K, Brooks DJ, et al. Comparison of methods for analysis of clinical [¹¹C]raclopride studies. J Cereb Blood Flow Metab 1996; 16:42–52.

28. Gunn RN, Lammertsma AA, Hume SP, Cunningham VJ. Parametric imaging of ligand-receptor binding in PET using a simplified reference region model. Neuroimage 1997;6:279–87.

29. Wu Y, Carson RE. Noise reduction in the simplified reference tissue model for neuroreceptor functional imaging. J Cereb Blood Flow Metab 2002;22:1440–52.

30. Ichise M, Ballinger JR, Golan H, Vines D, Luong A, Tsai S, et al. Noninvasive quantification of dopamine D2 receptors with Iodine-123-IBF SPECT. J Nucl Med 1996;37(3): 513–20.

31. Ichise M, Liow JS, Lu JQ, Takano A, Model K, Toyama H, et al. Linearized reference tissue parametric imaging methods: application to [¹¹C]DASB positron emission tomography studies of the serotonin transporter in human brain. J Cereb Blood Flow Metab 2003;23:1096–112.

32. Ikoma Y, Suhara T, Toyama H, Ichimiya T, Takano A, Sudo Y, et al. Quantitative analysis for estimating binding potential of the brain serotonin transporter with [¹¹C]McN5652. J Cereb Blood Flow Metab 2002;22:490–501.

33. Sokoloff L, Reivich M, Kennedy C, Des Rosiers MH, Patlak CS, Pettigrew KD, et al. The [14C]deoxyglucose method for the measurement of local cerebral glucose utilization: theory, procedure, and normal values in the conscious and anesthetized albino rat. J Neurochem 1977;28:897–916.

34. Phelps ME, Huang SC, Hoffman EJ, Selin C, Sokoloff L, Kuhl DE. Tomographic measurement of local cerebral glucose metabolic rate in humans with (F-18)2-fluoro-2-deoxy-D-glucose: validation of method. Ann Neurol 1979;6:371–88.

35. Dhawan V, Moeller JR, Strother SC, Evans AC, Rottenberg DA. Effect of selecting a fixed dephosphorylation rate on the estimation of rate constants and rCMRGlu from dynamic [¹⁸F]Fluorodeoxyglucose/PET data. J Nucl Med 1989;30: 1483–8.

36. Taguchi A, Toyama H, Kimura Y, Senda M, Uchiyama A. Comparison of the number of parameters using nonlinear iteration methods for compartment model analysis with ¹⁸F-FDG brain PET. Kaku Igaku 1997;34:25–34.

37. Huang SC, Yu DC, Barrio JR, Grafton S, Melega WP, Hoffman JM. Kinetics and modeling of L-6-[18F]fluoro-DOPA in human positron emission tomographic studies. J Cereb Blood Flow Metab 1991;11:898–913.

38. Hoshi H, Kuwabara H, Leger G, Cumming P, Guttman M, Gjedde A. 6-[18F]fluoro-L-DOPA metabolism in living human brain: a comparison of six analytical methods. J Cereb Blood Flow Metab 1993;13:57–69.

39. Cumming P, Gjedde A. Compartmental analysis of Dopa decarboxylation in living brain from dynamic positron emission tomograms. Synapse 1998;29:37–61.

40. Huang SC, Phelps ME, Hoffman EJ, Sideris K, Selin CJ, Kuhl DE. Noninvasive determination of local cerebral metabolic rate of glucose in man. Am J Physiol 1980;238:E69–82.

41. Carson RE, Huang SC, Green MV. Weighted integration method for local cerebral blood flow measurements with positron emission tomography. J Cereb Blood Flow Metab 1986; 6:245–58.

42. Blomqvist G. On the construction of functional maps in positron emission tomography. J Cereb Blood Flow Metab 1984; 4:629–32.

43. Kimura Y, Naganawa M, Yamaguchi J, Takabayashi Y, Uchiyama A, Oda K, et al. MAP-based kinetic analysis for voxel-by-voxel compartment model estimation: detailed

imaging of the cerebral glucose metabolism using FDG. Neuroimage 2006;29:1203–11.

44. Turkheimer FE, Aston JA, Banati RB, Riddell C, Cunningham VJ. A linear wavelet filter for parametric imaging with dynamic PET. IEEE Trans Medical Imaging 2003;22:289–301.

45. Patlak CS, Blasberg RG. Graphical evaluation of blood-to-brain transfer constants from multiple-time uptake data: generalizations. J Cereb Blood Flow Metab 1985;5:584–90.

46. Lucignani G, Schmidt KC, Moresco RM, Striano G, Colombo F, Sokoloff L. Measurement of regional cerebral glucose utilization with fluorine-18-FDG and PET in heterogeneous tissue: theoretical considerations and practical procedure. J Nucl Med 1993;34:360–9.

47. Yu DC, Huang SC, Barrio JR, Phelps ME. The assessment of the non-equilibrium effect in the "Patlak analysis" of Fdopa PET studies. Phys Med Biol 1995;40:1243–54.

48. Millet P, Delforge J, Pappata S, Syrota A, Cinotti L. Error analysis on parameter estimates in the ligand-receptor model: application to parameter imaging using PET data. Phys Med Biol 1996;41:2739–56.

49. Watabe H, Endres CJ, Breier A, Schmall B, Eckelman WC, Carson RE. Measurement of dopamine release with continuous infusion of [^{11}C]raclopride: optimization and signal-to-noise considerations. J Nucl Med 2000;41:522–30.

50. Turkheimer F, Sokoloff L, Bertoldo A, Lucignani G, Reivich M, Jaggi JL, et al. Estimation of compartment and parameter distribution in spectral analysis. J Cereb Blood Flow Metab 1998;18:1211–22.

51. Kukreja SL, Gunn RN. Bootstrapped DEPICT for error estimation in PET functional imaging. Neuroimage 2004;21:1096–104.

52. Ogden RT, Tarpey T. Estimation in regression models with externally estimated parameters. Biostatistics 2006;7:115–29.

53. Ogden RT, Ojha A, Erlandsson K, Oquendo MA, Mann JJ, Parsey RV. In vivo quantification of serotonin transporters using [(11)C]DASB and positron emission tomography in humans: modeling considerations. J Cereb Blood Flow Metab 2007;27:205–17.

54. Efron B, Tibshirani RJ. An introduction to the bootstrap. New York: Chapman and Hall; 1993.

55. Buvat I. A non-parametric bootstrap approach for analyzing the statistical properties of SPECT and PET images. Phys Med Biol 2002;47:1761–75.

Original article

Body-contour versus circular orbit acquisition in cardiac SPECT: Assessment of defect detectability with channelized Hotelling observer

Antti Sohlberg[a], Hiroshi Watabe[a], Miho Shidahara[b] and Hidehiro Iida[a]

Background The resolution of a gamma camera is depth-dependent and worsens with increasing distance to the camera resulting in a loss of fine details in SPECT images. A common approach to reduce the effects of this resolution loss is to utilize body-contour acquisition orbits. Even though body-contour orbits can improve resolution of reconstructed images their effect on lesion detection is not well known.

Objective To investigate whether body-contour orbits offer better defect detection performance than circular orbits in cardiac SPECT.

Methods The mathematical cardiac torso (MCAT) phantom was used to model ^{99m}Tc-sestamibi uptake. A total of four phantoms (two male and two female) with eight defects (four locations and two sizes) were generated and projection data were simulated using an analytical projector with attenuation, scatter, collimator response and acquisition orbit modelling. The circular and body-contour projections were reconstructed using the OSEM algorithm with/without collimator response compensation. Defect detection performance was assessed by calculating area under the receiver operating characteristic (ROC) curve for channelized Hotelling observer.

Results The defect detection performance of circular and body-contour acquisition was very similar and the

difference in the area under the ROC curve between the orbits was not statistically significant with or without collimator response compensation. The collimator response compensation, on the other hand, was noticed to be valuable and it provided significantly better defect detection performance than reconstruction without it regardless of the acquisition orbit type.

Conclusions We conclude that by replacing circular orbit with more complex body-contour orbit will not lead to statistically significant increase in defect detection performance in cardiac SPECT. *Nucl Med Commun* 28:937–942 © 2007 Wolters Kluwer Health | Lippincott Williams & Wilkins.

Introduction

The resolution of a gamma camera is depth dependent, which results in a loss of fine details in SPECT images. In order to reduce the effects of this depth dependency, body-contour acquisition orbits are often applied. Body-contour orbits improve the resolution by minimizing the object-to-detector distance and can provide approximately 1–2 mm improvement in resolution without any loss in sensitivity, when projection data is acquired with parallel hole collimators. Utilization of body-contour orbits is, however, complicated by the more complex acquisition process, especially if automatic contour tracking is used, and by the fact that body-contour orbits might be more prone to image artefacts than circular orbits [1,2]. These artefacts are generated due to resolution non-uniformity among different projections

and their severity depends on the geometry of the orbit and also on orientation of the target in the field of view [3,4].

Another approach to reduce the depth-dependent blurring is to apply collimator response compensation in reconstruction. Several investigators have indicated that significant improvements in image quality can be achieved when collimator response compensation is applied during reconstruction [5–8]. Collimator response modelling might also be beneficial when combined with body-contour orbits, because in addition to its resolution enhancement capabilities collimator response correction increases uniformity of resolution and could therefore reduce the artefacts, which have been reported to reduce the quality of body-contour studies.

Image quality obtained with different acquisition and reconstruction configurations is usually assessed with traditional metrics such as resolution and contrast. Even though these metrics are easy to apply and understand they are not necessarily good predictors of defect detection performance, which is the primary concern in cardiac SPECT. In this study the channelized Hotelling observer (CHO), which has shown to correlate well with human observer performance [9], was used to compare body-contour and circular orbits with and without collimator response compensation. The goal was to determine whether body-contour orbits could offer better defect detection performance in cardiac SPECT studies than circular orbits and to find the optimal acquisition–reconstruction method combination.

Materials and methods
Phantoms
The mathematical cardiac torso (MCAT) phantom [10,11] was used to simulate ^{99m}Tc-sestamibi distribution and non-uniform attenuation in the chest region. Four different phantoms, large female/male and small female/male, were generated each with eight different defects (Fig. 1). The lateral and antero-posterior sizes were 38 cm and 26 cm for the large phantoms and 32 cm and 24 cm for the small phantoms. The relative activities per voxel assigned to myocardium, liver, kidney, spleen, lung and rest of the body were 100, 50, 100, 80, 5 and 2.5. The defects had 90° or 120° angular extent, approximately

2.5 cm length and they were simulated with 20% contrast with respect to healthy myocardium.

Projection data simulation
Noise-free projection data was simulated using an analytical projector. Attenuation was simulated with the MCAT attenuation maps and collimator response was modelled according to the method by Metz [12]. A high-resolution low-energy parallel hole collimator with 4.0 cm hole length and 0.18 cm hole radius was used in the simulations. Circular hole shape was assumed which allowed the collimator point-spread function to be calculated analytically according to:

$$g(r,D) = 2\cos^{-1}\left(\frac{|r_T|}{2R}\right) - \frac{|r_T|}{R}\sqrt{1 - \frac{|r_T|^2}{4R^2}}, \quad (1)$$

where r is the distance in the detection plane from the intersection of the line perpendicular to the detection plane containing the source, D perpendicular distance from collimator to the source, R the radius of collimator hole and r_T the displacement of the centres of the projected aperture functions from the front face and back face of the collimator [13]. r_T is given by

$$r_T = r\frac{L}{D+L+C}, \quad (2)$$

where L is the collimator hole length and C the distance from back of the collimator to the detector crystal. Scatter was included using the method by Hutton [14,15]. Hutton's method consists of three steps. In the

Fig. 1

Top row: Example transverse slices of the MCAT phantoms used in the simulations. Bottom row: Example short-axis slices illustrating defect locations (defect contrast was enhanced for displaying purposes).

first step the activity distribution is convolved with monoexponential scatter kernels (exp $\alpha(d_s)r_s$), whose slopes $\alpha(d_s)$ depend on the depth in tissue (d_s). In the second step the convolved emission distribution is scaled using transmission-dependent scatter-to-true scatter fraction SF:

$$SF = A - B \left(e^{-\sum_{i=j}^{skin} \mu_k \Delta} \right)^\gamma - 1, \qquad (3)$$

where μ_k is the linear attenuation coefficient for voxel k, Δ the voxel size and parameters A, B and γ are fitting parameters obtained from experiment [14]. Scatter projections are finally obtained in the third step by forward projecting the convolved and scaled activity distribution at each projection angle.

Projection data was generated for 128 angles over 360° arc using 256 × 256 projection matrix and 0.156 cm pixel size. The radius of rotation for the body-contour orbits, at each projection angle, was determined by tracking the distance from the centre of rotation to the surface of the attenuation map of each four phantoms and circular orbit's radius of rotation was set to the maximum radius found in the corresponding body-contour orbit study. After simulation the projections were collapsed into 64 × 64 matrix size and Poisson noise was added. Projections were scaled so that the number of total counts was approximately 3.0 MCts. A total of 480 noisy projection data sets (four phantoms × eight defects × 15 noise realizations) with defect and 480 projection data sets (four phantoms × 120 noise realizations) without defect were generated for both orbits.

Reconstruction and post-processing

Reconstructions were performed using OSEM algorithm [16]. The projectors in our OSEM implementation were rotation based [17] and the rotation was performed using bilinear interpolation. Attenuation correction was included into the algorithm by rotating the attenuation map with the reconstruction volume during the reconstruction and applying each voxel the appropriate attenuation factor, which was calculated by summing the attenuation map along perpendicular lines from the volume elements to the detector. Original attenuation maps were blurred using a three-dimensional (3-D) Gaussian kernel with 1.0 cm full width at half maximum (FWHM) before they were applied in reconstruction in order to make attenuation compensation more realistic. Collimator response compensation was implemented by blurring each image plane at a different distance from the detector with a separable two-dimensional Gaussian kernel, whose FWHM was calculated assuming a linear model

$$FWHM(D) = \alpha + \beta D, \qquad (4)$$

for the decrease of resolution as a function of distance (D) from the detector. The α and β parameters were obtained by

simulating point sources at different distance from the collimator using the analytic projector described in previous section. FWHMs of these measurements were calculated and the linear model in Equation 4 was fitted to the measurements. It is worthwhile to note that collimator response compensation was performed using a different method that was used to simulate the projection data. This approach should provide more realistic results with collimator correction, which are not 'too good' due to the complete match of the projectors used in generation of the projection data and reconstruction. Correction for scatter was not performed.

Every noisy circular and body-contour projection data set was reconstructed with/without collimator response compensation using 32 subsets and two iterations. Reconstructed images were post-filtered with 3-D Gaussian filter with 1.25 cm FWHM. These reconstruction/post-filtering parameters have shown to provide near optimal defect detection performance in previous studies [18,19]. After filtering, images were realigned into short-axis slices and a single slice through the centre of the defect (for defect absent images the corresponding slice) was extracted for further analysis.

Channelized Hotelling observer and receiver operating characteristic analysis

Defect detection performance is most often measured using human observers. In these studies observers are shown a large number of images with and without defects acquired/reconstructed using the methods, which are to be compared against each other. The observers rate the existence of a defect, e.g., with a continuous scale from 0 (defect definitely absent) to 100 (defect definitely present). These ratings are then used to generate a receiver operating characteristic (ROC) curves, which plot the true positive fraction (fraction of images correctly classified as defect present) of the ratings against the false positive fraction (fraction of images falsely classified as defect present). The area under the ROC curve can be used as a measure of defect detection performance. The human observer studies are, however, often too time-consuming and expensive to perform and therefore computer observers such as the channelized Hotelling observer have been developed.

The CHO comes from signal-detection theory and its derivation is beyond the scope of this paper, but can be found elsewhere [20]. The following explains how CHO was applied in this work. The test statistic (λ), which is analogous to the rating obtained in a human observer study, was calculated for the CHO as

$$\lambda = h^T \bullet g, \qquad (5)$$

where h^T is the CHO, g is the feature vector and superscript T denotes transpose operation. The feature vector was obtained by processing the short-axis slice under testing by frequency selective channels, which

have been added to computer observers to mimic human visual processing of images [18]. In this study four rotationally symmetric channels with 1/64–2/64, 2/64–4/64, 4/64–8/64 and 8/64–16/64 cycles/pixel passbands were used. The frequency channels were shifted to each defect centre (shift was performed also for defect absent images) with a phase shift and the channels were converted into spatial domain with inverse Fourier transform. The CHO was calculated as

$$h^T = (\langle g_1 \rangle - \langle g_2 \rangle)^T S_{II}^{-1}, \tag{6}$$

where $\langle g_1 \rangle$ is the mean feature vector for defect present images, $\langle g_2 \rangle$, mean feature vector for defect absent images and S_{II} the intraclass scatter matrix [18,21]. First half of the short axis slices for each orbit/reconstruction method combination were used to calculate the CHO and the remaining half of the images were used to obtain the actual test statistics. Each receiver operating characteristic (ROC) curve was therefore estimated from the rating data of 240 defects present (four phantoms × eight defects × 15 noise realizations ÷ 2) and 240 defect absent (four phantoms × 120 noise realizations ÷ 2) images. The ROC curves and areas under the curves (AUC) were obtained using the ROCKIT software (http://www-radiology.uchicago.edu/krl).

Results

The results of the acquisition orbit comparison are presented in Table 1 and Fig. 2. As can be seen body-contour orbit offers slightly better defect detection performance than circular orbit when collimator response compensation is not applied, but the difference in the AUC values between the two orbits is not statistically significant at $P = 0.05$ level. Interestingly circular orbit performs better with collimator response correction than body-contour acquisition. This is probably due to the fact that the reconstruction voxel size is quite large compared to the FWHM of the Gaussian that is used to model the collimator response, which might lead to relatively crude presentation of the blurring kernels. With body-contour orbits this phenomenon has even bigger effect, because the imaging distance is shorter and thus the Gaussian kernels are narrower. It is, however, important to note that the difference in AUCs between circular and body-contour orbits when collimator response compensation is applied is not statistically significant.

Table 1 Comparison between circular/body-contour acquisition and reconstruction with/without collimator response compensation (coll)

Method 1	Method 2	AUC 1	AUC 2	P
Circular w/o coll	Contour w/o coll	0.856	0.862	0.358
Circular w coll	Contour w coll	0.901	0.894	0.325
Circular w/o coll	Circular w coll	0.856	0.901	<0.001
Contour w/o coll	Contour w coll	0.862	0.894	<0.001

Fig. 2
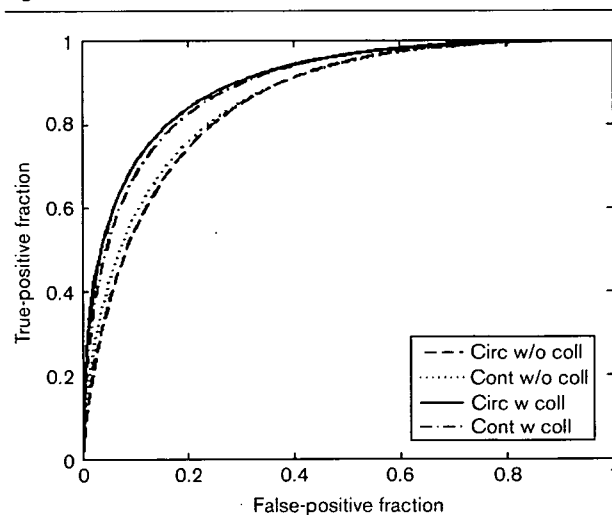
ROC curves for circular and body-contour orbit studies reconstructed with/without collimator response compensation (coll).

Figure 3 shows representative images from circular and body-contour orbit studies. When comparing individual images it is worthwhile keeping in mind that circular and body-contour images correspond to different projection data noise realizations and thus some of the differences seen in images might be due to noise and not different acquisition orbits. Overall there are no large differences among the images. Reconstructions with collimator response compensation provide smoother and thus perhaps more visually pleasing image quality than reconstruction without correction.

Discussion

Body-contour acquisition orbits have the ability to increase resolution and contrast, but their effect on defect detection performance in cardiac SPECT is not well known. This study compared circular and body-contour orbits using CHO and ROC analysis. The defect detectability with the two orbits was noticed to be quite similar. The difference in areas under the ROC curve was 0.006 for reconstruction without collimator modelling and 0.007 with collimator modelling. Even though the body-contour orbit increased the area under curve, when collimator response correction was not applied, it could not provide statistically significant improvement in defect detection performance. Similar findings were made by White et al. [22], who reported that circular and body-contour orbits do not differ significantly in terms of defect extent, reversibility or size assessment.

Body-contouring adds extra complexity to acquisition procedure and may generate additional artefacts as

Fig. 3
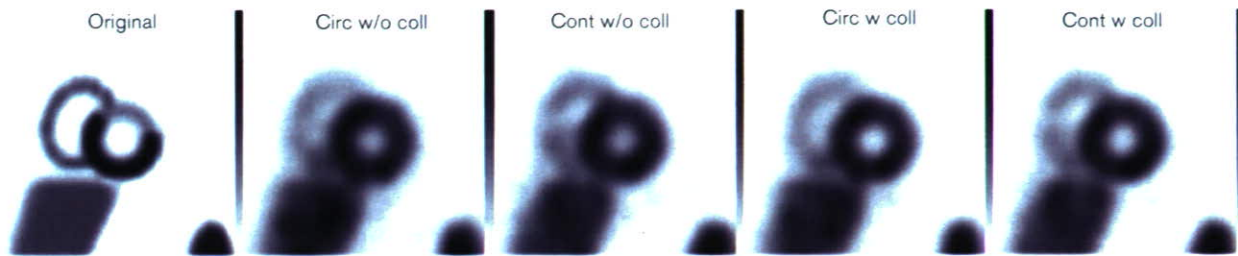
Example reconstructed short-axis slices obtained with circular and body-contour orbit with/without collimator response compensation (coll). Original image has enhanced defect contrast.

explained in Introduction. We proposed that collimator response modelling might reduce these artefacts and could therefore offer better image quality. No significant acquisition orbit related artefacts were, however, noticed in this study. The absence of artefacts might be partly related to the utilization of 360° acquisitions orbits, which have shown to be less prone to errors than 180° orbits [1]. Moreover, many of the studies that have reported artefacts with body-contour orbits have used filtered back-projection (FBP) as reconstruction method, whereas we used OSEM, which is known to provide images with higher quality than FBP. Even though the body-contour orbit and collimator response compensation combination did not outperform circular orbit with collimator response correction, the collimator response compensation itself was noticed to be very valuable. Collimator response correction increased AUC by 0.045 for circular and by 0.032 for body-contour orbit. Both improvements were statistically significant. Similar findings have been presented before [23,24].

This study has three primary limitations, which are discussed next. First the acquisition orbit comparison was performed using simulated rather than real patient data and thus might not provide the level of realism of a clinical study. On the other hand the complete lack of patient motion and other such factors that deteriorate the quality of clinical SPECT studies allowed us to concentrate only to differences due to acquisition orbits. Moreover, the exact knowledge of the size, shape and location of the defects made the detection performance measurements reliable. This investigation would have been quite difficult to perform as a clinical study: In order to obtain statistically reliable results a large patient population with, for example, angiography information would have been needed. Each patient participating in the study would have also needed two sequential SPECT scans, which would have increased patient discomfort and risk for motion artefacts, in addition to halving the throughput of our scanner.

Second, the simulations in this study were performed using an analytical projection code instead of a Monte Carlo simulator. An analytical simulator was chosen because many of the Monte Carlo packages available do not directly support acquisitions with non-symmetrical body-contour orbits. Our analytical simulator, on the other hand, allows easy modelling of the acquisition orbit. The collimator response modelling in our simulator is performed using similar method as with the popular SIMIND [25] and SIMSET [26] Monte Carlo packages. Thus the only larger difference between our analytical and Monte Carlo simulators is the incorporation of scatter. Scatter modelling in our simulator was implemented using Hutton's method and although this method produces relatively crude scatter approximation it still increases the realism of the projection data. We also believe that accurate scatter modelling is not so important in this study, because we are studying resolution effects.

Third, the image quality was assessed using computer observer instead of human observers. We chose computer observers, because human observer studies are time-consuming and expensive to perform. The CHO used in this work has, however, shown to correlate well with human observers [9,27]. CHOs can also provide much better prediction of human performance than metrics like resolution, contrast and noise level, which are often used to compare acquisition and reconstruction methods.

In conclusion, circular and body-contour orbits offer quite similar defect detection performance and thus the selection of acquisition orbit is of not vital importance in cardiac SPECT. Collimator response compensation, on the other hand, significantly increases defect detectability regardless of acquisition type and should therefore be applied in reconstruction whenever available.

Acknowledgement

References

1 Eisner RL, Nowak DJ, Pettigrew R, Fajman W. Fundamentals of 180° acquisition and reconstruction in SPECT imaging. *J Nucl Med* 1986; 27:1717–1728.

2 O'Connor MK, Hruska CB. Effect of tomographic orbit and type of rotation on apparent myocardial activity. *Nucl Med Commun* 2005; 26:25–30.

3 Maniawski PJ, Morgan HT, Wackers FJT. Orbit-related variation in spatial resolution as a source of artifactual defects in thallium-201 SPECT. *J Nucl Med* 1991; 32:871–875.

4 Abufadel A, Eisner RL, Schafer RW. Differences due to collimator blurring in cardiac images with use of circular and elliptic camera orbits. *J Nucl Cardiol* 2001; 8:458–465.

5 Hutton BF, Lau YH. Application of distance-dependent resolution compensation and post-reconstruction filtering for myocardial SPECT. *Phys Med Biol* 1998; 43:1679–1693.

6 Lau YH, Hutton BF, Beekman FJ. Choice of collimator for cardiac SPET when resolution compensation is included in iterative reconstruction. *Eur J Nucl Med* 2001; 28:39–47.

7 Zeng GL, Gullberg GT. Frequency domain implementation of the three-dimensional geometric point response correction in SPECT imaging. *IEEE Trans Nucl Sci* 1992; 39:1444–1453.

8 Zeng GL, Gullberg GT, Bai C, Christian PE, Trisjono F, Di Bella EVR, et al. Iterative reconstruction of fluorine-18 SPECT using geometric point response correction. *J Nucl Med* 1998; 39:124–130.

9 Wollenweber SD, Tsui BMW, Lalush DS, Frey EC, LaCroix KJ, Gullberg GT. Comparison of Hotelling observer models and human observers in defect detection from myocardial SPECT imaging. *IEEE Trans Nucl Sci* 1999; 46:2098–2103.

10 Tsui BMW, Zhao XD, Gregoriou GK, Lalush DS, Frey EC, Johnston RE, et al. Quantitative cardiac SPECT reconstruction with reduced image degradation due to patient anatomy. *IEEE Trans Nucl Med* 1994; 41:2838–2844.

11 Pretorius PH, King MA, Tsui BMW, LaCroix KJ, Xia W. A mathematical model of motion of the heart for use in generating source and attenuation maps for simulating emission imaging. *Med Phys* 1999; 26:2323–2332.

12 Metz CE, Atkins FB, Beck RN. The geometric transfer function component for scintillation camera collimators with straight parallel holes. *Phys Med Biol* 1980; 25:1059–1070.

13 Frey EC, Tsui BMW, Gullberg GT. Improved estimation of the detector response function for converging beam collimators. *Phys Med Biol* 1998; 43:941–950.

14 Hutton BF, Osiecki A, Meikle SR. Transmission-based scatter correction of 180° myocardial single-photon emission tomographic studies. *Eur J Nucl Med* 1996; 23:1300–1308.

15 Hutton BF, Baccarne V. Efficient scatter modelling for incorporation in maximum likelihood reconstruction. *Eur J Nucl Med* 1998; 25:1658–1665.

16 Hudson HM, Larkin RS. Accelerated image reconstruction using ordered subsets of projection data. *IEEE Trans Med Imag* 1994; 13:601–609.

17 Di Bella EVR, Barclay AB, Eisner RL, Schafer RW. A comparison of rotation-based methods for iterative reconstruction algorithms. *IEEE Trans Nucl Sci* 1996; 43:3370–3376.

18 Frey EC, Gilland KL, Tsui BMW. Application of task-based measures of image quality to optimization and evaluation of three-dimensional reconstruction-based compensation methods in myocardial perfusion SPECT. *IEEE Trans Med Imag* 2002; 21:1040–1050.

19 Narayanan MV, Gifford HC, King MA, Pretorius PH, Farncombe TH, Bruyant P, et al. Optimization of iterative reconstructions of ^{99m}Tc cardiac SPECT studies using numerical observers. *IEEE Trans Nucl Sci* 2002; 5:2355–2360.

20 Myers KJ, Barrett HH. Addition of a channel mechanism to the ideal-observer model. *J Opt Soc Am A* 1987; 4:2447–2457.

21 Shidahara M, Inoue K, Maruyama M, Watabe H, Taki Y, Goto R, et al. Predicting human performance by channelized Hotelling observer in discriminating between Alzheimer's dementia and controls using statistically processed brain perfusion SPECT. *Ann Nucl Med* 2006; 20:605–613.

22 White MP, Russell A, Mascitelli VA, Morris RS, Shehata AR, Heller GV. Clinical comparison of circular versus noncircular acquisition using technetium-99m myocardial perfusion SPECT imaging. *J Nucl Med Technol* 1997; 25:37–40.

23 He X, Links JM, Gilland GL, Tsui BMW, Frey EC. Comparison of 180° and 360° acquisition for myocardial perfusion SPECT with compensation for attenuation, detector response, and scatter: Monte Carlo and mathematical observer results. *J Nucl Cardiol* 2006; 13:345–353.

24 Narayanan MV, King MA, Pretorius PH, Dahlberg ST, Spencer F, Simon E, et al. Human-observer receiver-operating-characteristic evaluation of attenuation, scatter, and resolution compensation strategies for ^{99m}Tc myocardial perfusion imaging. *J Nucl Med* 2003; 44:1725–1734.

25 Ljungberg M, Strand S-E. A Monte Carlo program for the simulation of scintillation camera characteristics. *Comput Methods Programs Biomed* 1989; 29:257–272.

26 Harrison RL, Vannoy SD, Haynor DR, Gillispie SB, Kaplan MS, Lewellen TK. Preliminary experience with the photon history generator module of a public-domain simulation system for emission tomography. *Conf Rec IEEE Nucl Sci Symp* 1993; 1154–1158.

27 Sankaran S, Frey EC, Gilland KL, Tsui BMW. Optimum compensation method and filter cutoff frequency in myocardial SPECT: a human observer study. *J Nucl Med* 2002; 43:432–438.

Stroke

American Stroke Association

A Division of American
Heart Association

Delayed Postischemic Treatment With Fluvastatin Improved Cognitive Impairment After Stroke in Rats

Munehisa Shimamura, Naoyuki Sato, Masataka Sata, Hitomi Kurinami, Daisuke Takeuchi, Kouji Wakayama, Takuya Hayashi, Hidehiro Iida and Ryuichi Morishita

The online version of this article, along with updated information and services, is located on the World Wide Web at:
http://stroke.ahajournals.org

Delayed Postischemic Treatment With Fluvastatin Improved Cognitive Impairment After Stroke in Rats

Munehisa Shimamura, MD, PhD; Naoyuki Sato, MD, PhD; Masataka Sata, MD, PhD;
Hitomi Kurinami, MD; Daisuke Takeuchi, MD; Kouji Wakayama, MD; Takuya Hayashi, MD, PhD;
Hidehiro Iida, MD, PhD; Ryuichi Morishita, MD, PhD

Background and Purposes—Recent clinical evidences indicate that statins may have beneficial effects on the functional recovery after ischemic stroke. However, the effect of delayed postischemic treatment with statins is still unclear. In the present study, we evaluated the effects of fluvastatin in the chronic stage of cerebral infarction in a rat model.

Methods—Rats exposed to permanent middle cerebral artery occlusion were treated for 3 months with fluvastatin beginning from 7 days after stroke. MRI, behavioral analysis, and immunohistochemistry were performed.

Results—Two months of treatment with fluvastatin showed the significant recovery in spatial learning without the decrease in serum total cholesterol level and worsening of infarction. Microangiography showed a significant increase in capillary density in the peri-infarct region in fluvastatin-treated rats after 3 months of treatment. Consistently, BrdU/CD31-positive cells were significantly increased in fluvastatin-treated rats after 7 days of treatment. MAP1B-positive neurites were also increased in the peri-infarct region in fluvastatin-treated rats. In addition, rats treated with fluvastatin showed the reduction of superoxide anion after 7 days of treatment and the reduction of $A\beta$ deposits in the thalamic nuclei after 3 months of treatment.

Conclusions—Thus, delayed postischemic administration of fluvastatin had beneficial effects on the recovery of cognitive function without affecting the infarction size after ischemic stroke. Pleiotropic effects of fluvastatin, such as angiogenesis, neuritogenesis, and inhibition of superoxide production and $A\beta$ deposition, might be associated with a favorable outcome. (***Stroke.*** 2007;38:000-000.)

Key Words: angiogenesis ■ cerebral infarct ■ microcirculation ■ statins

Despite conflicting data correlating cholesterol level with stroke, 2 early trials of HMG-CoA reductase inhibitors (statins) in patients after myocardial infarction patients showed a reduction in stroke risk as a secondary end point.[1] A meta-analysis of 9 statin intervention trials, which enrolled patients with coronary artery disease or those at high risk for coronary disease, demonstrated a 21% relative risk reduction for stroke after 5 years of treatment.[2] Another clinical evidence suggests that the commencement of statins within 4 weeks of a stroke results in a favorable 90-day outcome.[3] To clarify the effects of postischemic statin treatment, previous studies in which atorvastatin was started 1 day after stroke in rodents showed improvement of sensory motor deficit through induction of angiogenesis, neurogenesis, and synaptogenesis.[4,5] These pleiotropic effects of statins were shown to be the result of induction of vascular endothelial growth factor or brain-derived neurotrophic factor.[4] Additionally, the microvascular dysfunction in the posttreatment of stroke with recombinant human tissue-type plasminogen activator could

be reduced by statins in rodent model.[6] However, the effect of delayed treatment with statins after ischemic stroke is still unknown. From this viewpoint, we investigated whether chronic statin treatment beginning 7 days after ischemic stroke had influences on neurological deficits and pathophysiology after the permanent middle cerebral artery occlusion (MCAo) model in rats.

Materials and Methods

Surgical Procedure
Male Wistar rats (270 to 300 grams; Charles River; Kanagawa, Japan) were used in this study. The right MCA was occluded by placement of poly-L-lysine–coated 4-0 nylon, as described previously.[7]

Protocol for Treatment and Behavioral Tests
Ten rats were only anesthetized (sham operation) and 32 rats were subjected to MCAo (day 1). Based on neuromuscular function on day 7, the rats were divided equally into saline-treated (n=16) or fluvastatin-treated (n=16) groups. Fluvastatin (5 mg/kg per day;

provided by Novartis Pharma) or saline was given by gavage from day 7 to 100. We chose the dose (5 mg/kg per day), because a previous report showed that this dose could effectively induce angiogenesis in ischemic limb.[8] On day 55, neuromuscular function and locomotor activity were evaluated in the surviving rats. Then, cognitive function was examined by Morris water maze from day 56 to 63, because the effects of neuronal regeneration could be detected not in the early stage but in the chronic stage of ischemic brain such as 49 to 53 days after the insult.[9] On day 96, MRI was performed. On day 100, microangiography was performed.

MRI

High-resolution T1-weighted fast spin echo sequence images (repetition time [TR]=1500 ms; echo time [TE]=10.3 ms; field of view [FOV]=4×3 cm; matrix=256×192; slice thickness=1.5 mm; slice gap=0.5 mm; number of slices=16; number of excitation=10; total time=9.39 min) were obtained using a 3-T MRI scanner (Signa LX VAH/I; GE).

Sensory Motor Deficit and Locomotor Activity

Although there are various batteries for testing sensory motor deficit, we used a simple protocol.[10] For forelimb flexion, rats were held by the tail on a flat surface. Paralysis of the forelimbs was evaluated by the degree of left forelimb flexion. For torso twisting, rats were held by the tail on a flat surface. The degree of body rotation was checked. For lateral push, rats were pushed either left or right. Rats with right MCA occlusion showed weak or no resistance against a left push. For hind limb placement, one hind limb was removed from the surface. Rats with right MCA occlusion showed delayed or no replacement of the hind limb when it was removed from the surface.

Spontaneous activity was measured via the open field (0.69 m²). We set the sensor, which also put beams on the field, at 30 cm above the field. The number of count, which is when the animal crosses the beam, was measured for 30 minutes.

Morris Water Maze Task

A cylindrical tank 1.5 m in diameter was filled with water (25°C), and a transparent platform 15 cm in diameter was placed at a fixed position in the center of 1 of the 4 quadrants (O'Hara & Co, Ltd). In the hidden platform trials, we performed the tests 4 times per day for 4 days. When the rat could not reach the platform, the latency was set at 60 sec. In the visible platform trials, the tests were performed 4 times per day for 4 days. The acquired data were averaged per day.

Evaluation of Capillary Density

Using a recently developed microangiographic technique,[11] capillary density and blood–brain barrier leakage were evaluated in the cerebral cortex after MCA occlusion. The area or length of vessels was analyzed with an angiogenesis image analyzer (version 1.0; Kurabo).

Immunohistochemical Study: Bromodeoxyuridine Labeling

To identify newly formed DNA, saline-treated (n=5) and fluvastatin-treated (n=5) rats received injections of bromodeoxyuridine (BrdU, 50 mg/kg; Sigma-Aldrich, Saint Louis, Mo) intraperitoneally starting on day 7 twice per day until day 13. Rats were euthanized on day 14. After the sections (8-μm thickness) was fixed in 10% formaldehyde/MeOH neutral buffer solution and blocked, they were incubated with mouse monoclonal anti-rat CD31 antibody (1:100; BD Biosciences; San Jose, Calif), goat polyclonal anti-doublecortin (anti-DCX; Santa Cruz, Calif) antibody (1:100; Santa Cruz, Calif), mouse monoclonal anti-NeuN antibody (1:1000; Chemicon, Temecula, Calif), or mouse monoclonal anti-MAP1B antibody (1:100; Sigma-Aldrich), followed by anti-mouse goat fluorescent antibody (1:1000 for NeuN and MAP1B, 1:400 for CD31, Alexa Flour 546, Molecular Probes; Eugene, Ore) or anti-goat donkey fluorescent antibody (1:1000 for DCX Alexa Fluor 546). For double immunostaining, these sections were fixed again and incubated in 2 N HCl at 37°C for 30 minutes. After blocking, they were incubated with rat monoclonal

Table. Infarction Volume Calculated by MRI, Blood Pressure, and Serum Total Cholesterol

	Sham	MCAo + S	MCAo + F	P
Infarction volume in total rats (mm³)	...	283.8±23.9	278.4±26.4	0.851
Type of infarction in Figure 1a (N of rats)				0.828
A	...	12	11	...
B	...	3	3	...
C	...	1	2	...
Infarction volume (mm³) in type A rats	...	322.8±15.0	327.0±18.8	0.758
Systolic blood pressure (mm Hg) in type A rats				
Day 7	116.1±5.4	123.7±6.0	115.5±7.3	0.654
Day 56	146.5±4.7	148.3±2.7	136.1±5.2	0.132
Serum total cholesterol (mg/dl) in type A rats on day 56	85.9±5.6	75.3±3.5	73.5±2.7	0.949

Type A, low-intensity area seen in the dorsolateral and lateral portions of the neocortex and the entire caudate putamen; type B, low-intensity area seen in the dorsolateral and lateral portions of the neocortex and in part of the caudate putamen; type C, low-intensity area seen in part of the lateral neocortex and caudate putamen. MCAo + S, saline-treated rats after MCAo; MCAo + F, fluvastatin-treated rats after MCAo.

P, saline vs fluvastatin.

anti-BrdU antibody (1:200; Abcam, Cambridge, UK) followed by anti-rat goat fluorescent antibody (1:1000, Alexa Fluor 488). For immunohistochemical staining for Aβ, sections were pretreated for 30 minutes with hot (85°C) citrate buffer as described before.[12] Confocal images were acquired using an FV-300 (Olympus).

Quantitative Histological Analysis

To quantify the immunoreactivity for MAP1B and Aβ, the acquired image was analyzed by Image J (version 1.32; NIH).

Detection of Superoxide Anion in Brain Sections

Superoxide anion was detected on day 14 as described previously.[13] Because intact cortex showed red fluorescence, we calculated the ratio of fluorescence as follows: ratio of fluorescence=[fluorescence intensity in ischemic core or peri-infarct region]/[fluorescence intensity in intact region].

Statistical Analysis

All values are expressed as mean±SEM. To analyze the differences in the type of cerebral infarction, χ^2 test was performed. The latency, path length, and mean speed in Morris water maze and sensory motor deficits were analyzed by a 2-factor repeated-measure ANOVA. Post hoc analyses were performed, and the Scheffe test was applied to control the inflation in type I error. The value of the serum total cholesterol, the blood pressure, and the spontaneous activity was analyzed by Scheffe rules. The differences in the immunohistochemistry and the volume of infarction were assessed by Mann–Whitney *U* analyses. In all cases, *P*<0.05 was considered significant.

Results

Effects of Fluvastatin on Cognitive Impairment

To confirm the severity of cerebral infarction, all rats were examined by T1-weighted MRI after 89 days of treatment. Although the total volume of infarction calculated in T1-weighted images was not different between rats treated with
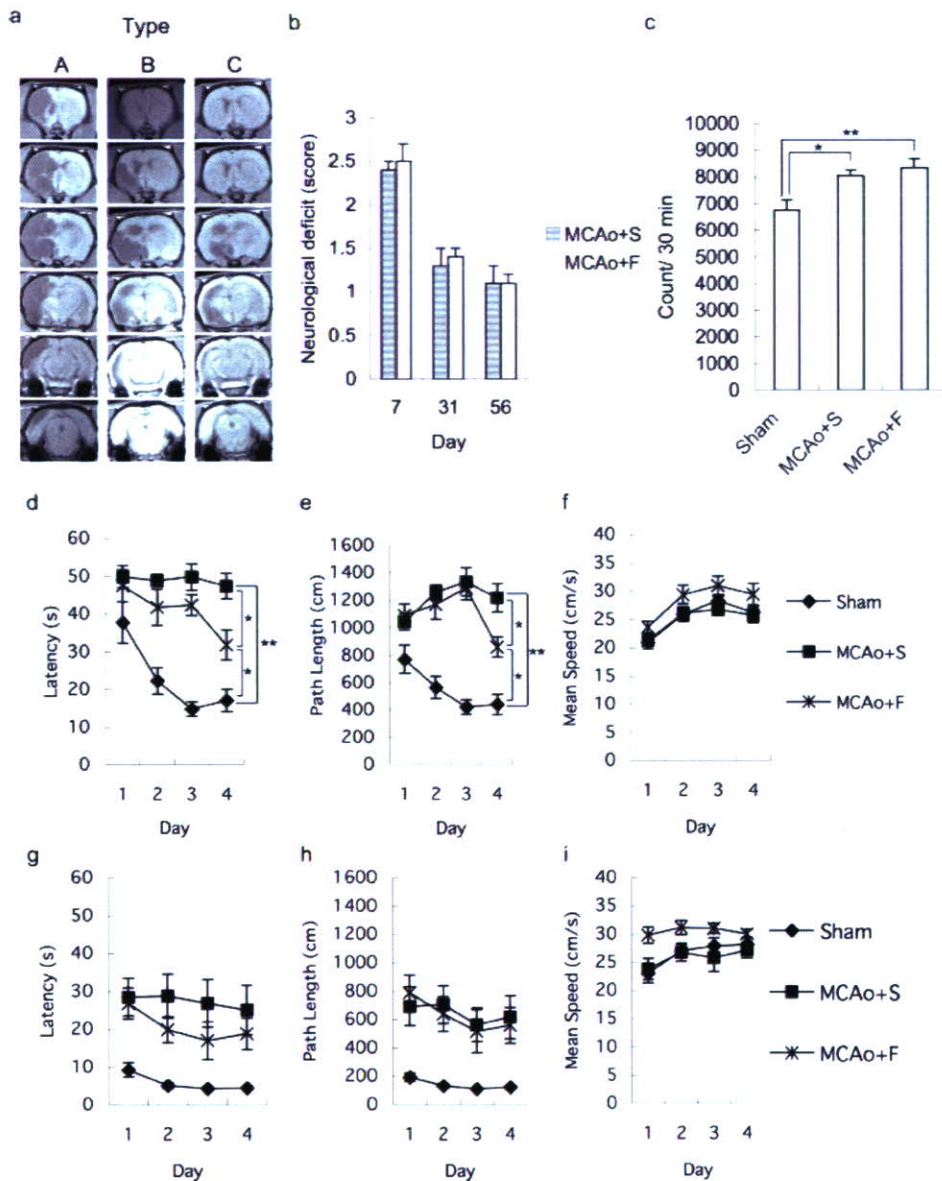
Figure 1. Typical T1-weighted image of coronal section of rat brain (a). The images were divided into 3 groups. Type A, low-intensity area seen in the dorsolateral and lateral portions of neocortex and the entire caudoputamen; type B, low-intensity area seen in the dorsolateral and lateral portions of neocortex and in part of the caudatoputamen; and type C, high-intensity area seen in part of the lateral neocortex and caudatoputamen. Sensory motor deficit (b). Spontaneous locomotor activity (c). Hidden platform test in Morris water maze. Each figure showed latency (d), path length (e), and mean speed (f). Days 1 to 4 indicate the trial day in the hidden platform test (56 to 59 days after middle cerebral artery occlusion). Visible platform test in Morris water maze. Each figure showed latency (g), path length (h), and mean speed (i). Days 1 to 4 indicate the day in the visible platform test (60 to 63 days after middle cerebral artery occlusion). MCAo+S indicates rats treated with saline after middle cerebral artery occlusion; MCAo+F, rats treated with fluvastatin after middle cerebral artery occlusion.

saline and fluvastatin (Table), the pattern of cerebral infarction was divided into 3 groups: type A, low-intensity area seen in the dorsolateral and lateral portions of the neocortex and the entire caudate putamen; type B, low-intensity area seen in the dorsolateral and lateral portions of the neocortex and in part of the caudate putamen; type C, low-intensity area seen in part of the lateral neocortex and caudate putamen (Figure 1a). In type C, most of the lateral neocortex was intact. To exclude the influence of the pattern of cerebral infarction on cognitive function, we focused on type A rats in the present study. The volume of cerebral infarction in type A

rats was not different between the groups (Table). Blood pressure and serum total cholesterol also showed no difference among the groups (Table).

Sensory motor deficit had spontaneously recovered to some extent by 8 weeks in both groups, and there was no difference (Figure 1b). Locomotor activity in rats subjected to MCAo was increased as compared with that in sham-operated rats, as described before,[14] but there was no significant difference between fluvastatin-treated and saline-treated rats (Figure 1c). In Morris water maze (Figure 1d-i), which examines spatial learning, there were significant differences
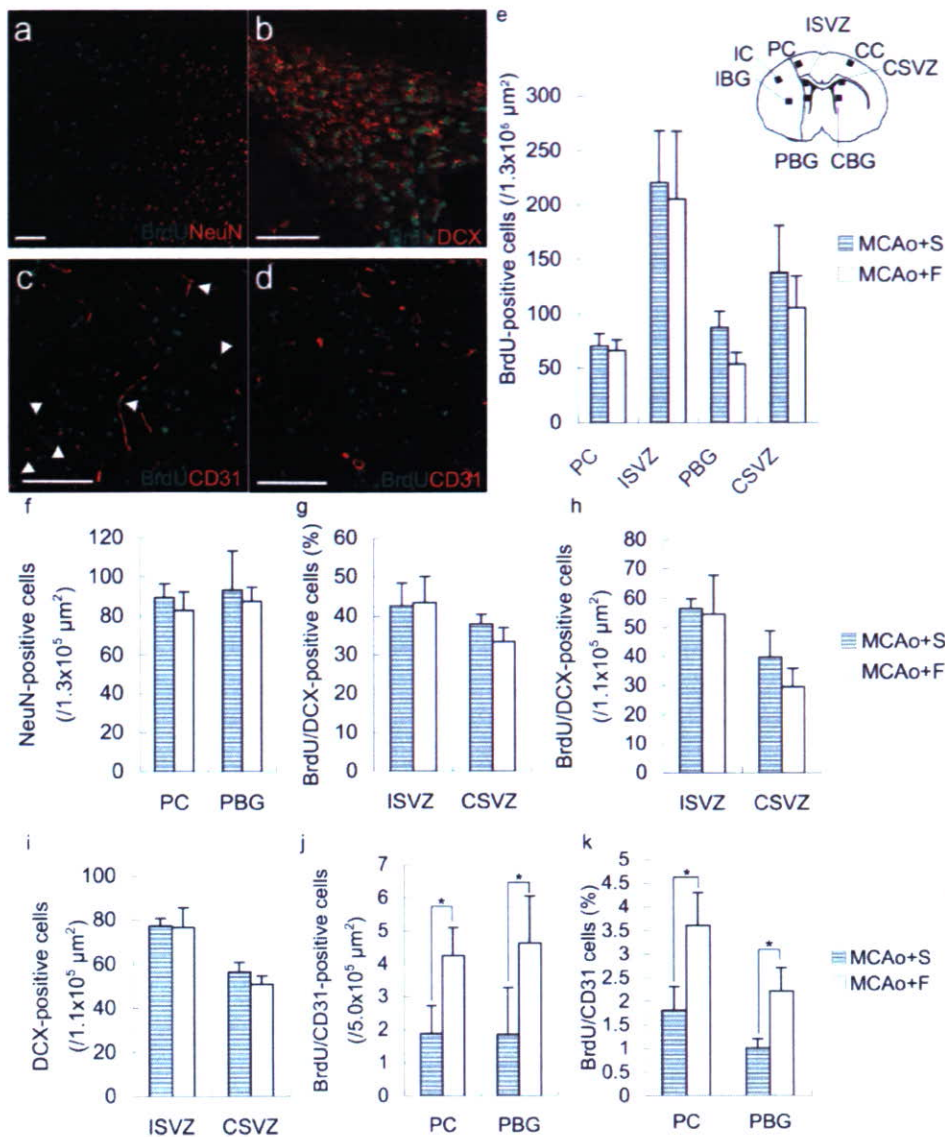
Figure 2. Representative images of immunohistochemical staining on day 14. Rats treated with fluvastatin (a through c), rats treated with saline (d). Although BrdU-positive cells were observed in the peri-infarct cortex (a), peri-infarct basal ganglia, and subventricular zone, these cells did not express NeuN (a), but expressed DCX in the subventricular zone (b). Fluvastatin-treated rats showed some BrdU/CD31-positive cells (arrows, c), although most BrdU-positive cells were negative for CD31 in saline-treated rats (d). The number of BrdU-positive cells (e), NeuN-positive cells (f), BrdU/DCX-positive cells (h), DCX-positive cells (i), and BrdU/CD31-positive cells (j); the percentage of BrdU/DCX-positive cells (g) or BrdU/CD31 cells (k) in total BrdU-positive cells. PC indicates peri-infarct cortex; PBG, peri-infarct basal ganglia; IC, infarcted cortex; IBG, ischemic basal ganglia; ISVZ, subventricular zone on infarcted side; CC, contralateral cortex, CSVZ, subventricular zone on contralateral side; CBG, contralateral basal ganglia (n=5 in each group, *P<0.05, bar=100 μm).

in the latency and path length in hidden platform test among the groups (supplemental Table I, available online at http://stroke.ahajournals.org). A significant difference was observed on day 4 between fluvastatin-treated and saline-treated rats (supplemental Table I). Also, there was a significant difference between sham and saline-treated rats (supplemental Table I). There was no significant difference both in swimming speed and visible platform test, which excluded the possible influence of visual loss, sensory motor deficit, and motivation on the results.[15] These data suggest that impaired spatial learning was improved by fluvastatin.

Histological Changes by Fluvastatin

Next, we studied whether fluvastatin had some influences on the histology. Initially, we focused on neurogenesis and angiogenesis. To examine neurogenesis, we measured BrdU-incorporated cells after injecting BrdU from day 7 to day 13. Although BrdU-positive cells were observed in the subventricular zone and peri-infarct region (Figure 2a to 2d), the total number did not differ between the groups (Figure 2e). Similarly, the density of NeuN-positive cells, as a marker of adult neurons, also did not differ between the groups (Figure 2f), whereas there were no BrdU/NeuN-positive cells in the
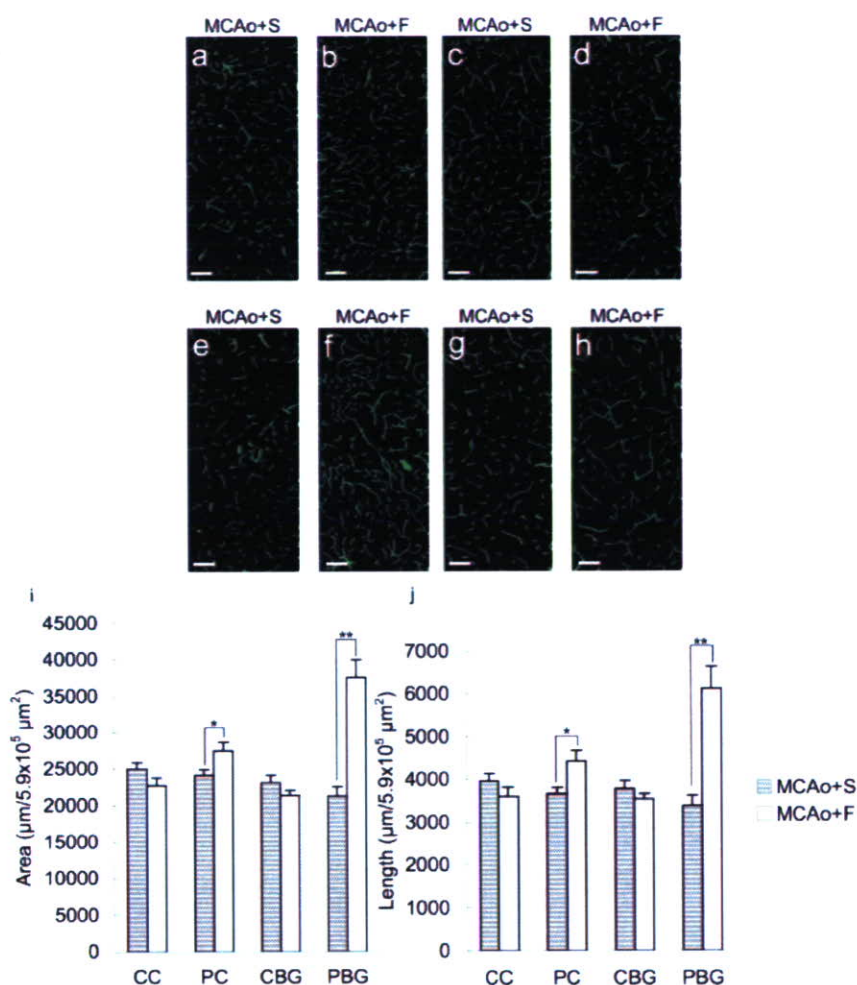
Figure 3. Microangiographic images using albumin-fluorescence isothiocyanate on day 100: (a and b) peri-infarct cortex; (c and d) contralateral cortex; (e and f) peri-infarct basal ganglia; (g and h) contralateral basal ganglia (bar=100 μm). Quantitative analysis (i and j) of microangiography. Rats treated with fluvastatin showed increased microvessels in the peri-infarct region (n=4 in each group, *P<0.05, **P<0.01).

peri-infarct cortex and subventricular zone (Figure 2a). Although some BrdU-positive cells expressing DCX, a marker for migrating neuroblasts, could be detected in subventricular zone (Figure 2b), the percentage in total BrdU-positive cells (Figure 2g) and the number (Figure 2h) did not differ between the groups. Also, the number of DCX-positive cells was same in the both groups (Figure 2i). There were no BrdU-positive cells expressing DCX in the cerebral cortex. Unexpectedly, these data suggest that neurogenesis was not enhanced by fluvastatin.

Thus, we further examined whether angiogenesis was affected by fluvastatin. In the peri-infarct cortex and basal ganglia, BrdU-positive cells that were positive for CD31 as a marker of endothelial cells could be detected (Figure 2c,2d). The number of BrdU/CD31-double-positive cells was significantly increased in fluvastatin-treated rats (Figure 2j). The percentage of BrdU/CD31-double-positive cells in total BrdU-positive cells was also increased in fluvastatin-treated rats (Figure 2k). Consistently, microangiography using FITC-conjugated albumin[11] also showed that microvessels were significantly increased in fluvastatin-treated rats only in the peri-infarct cortex and basal ganglia, without destruction of the blood–brain (Figure 3a to 3h). Quantitative analysis showed that the length and area of microvessels were also increased in the peri-infarct region, but not in the contralateral

cortex and contralateral basal ganglia, in rats treated with fluvastatin, at 3 months after stroke (Figure 3i,j).

Because recent reports showed that neurite outgrowth was observed in the peri-infarct region from 7 to 14 days after cerebral infarction,[16,17] we next examined the effect of fluvastatin on neurite outgrowth. Immunohistochemical staining showed that treatment with fluvastatin significantly increased the immunoreactivity of MAP1B, a marker of neurite outgrowth, in neurites[16,18] (Figure 4), although the number of MAP1B-positive cells was the same in both groups. These data implied that the fluvastatin might promote angiogenesis, resulting in improvement of the microcirculation, and neurite outgrowth.

One possible explanation for the enhanced angiogenesis and neurite outgrowth is a decrease in oxidative stress by fluvastatin. To assess oxidative stress, we evaluated superoxide production using dihydroethidium staining (Figure 5a to 5e). Superoxide anion was increased in the ischemic core as compared with the contralateral region at 2 weeks after MCA occlusion (Figure 5a,5c). However, rats treated with fluvastatin showed a significant reduction in superoxide anion especially in the ischemic core region, but not in the peri-infarct cortex and basal ganglia (Figure 5b,5d,5e).

Finally, we examined Aβ deposition in the thalamic nuclei, because previous reports showed that Aβ deposits in the
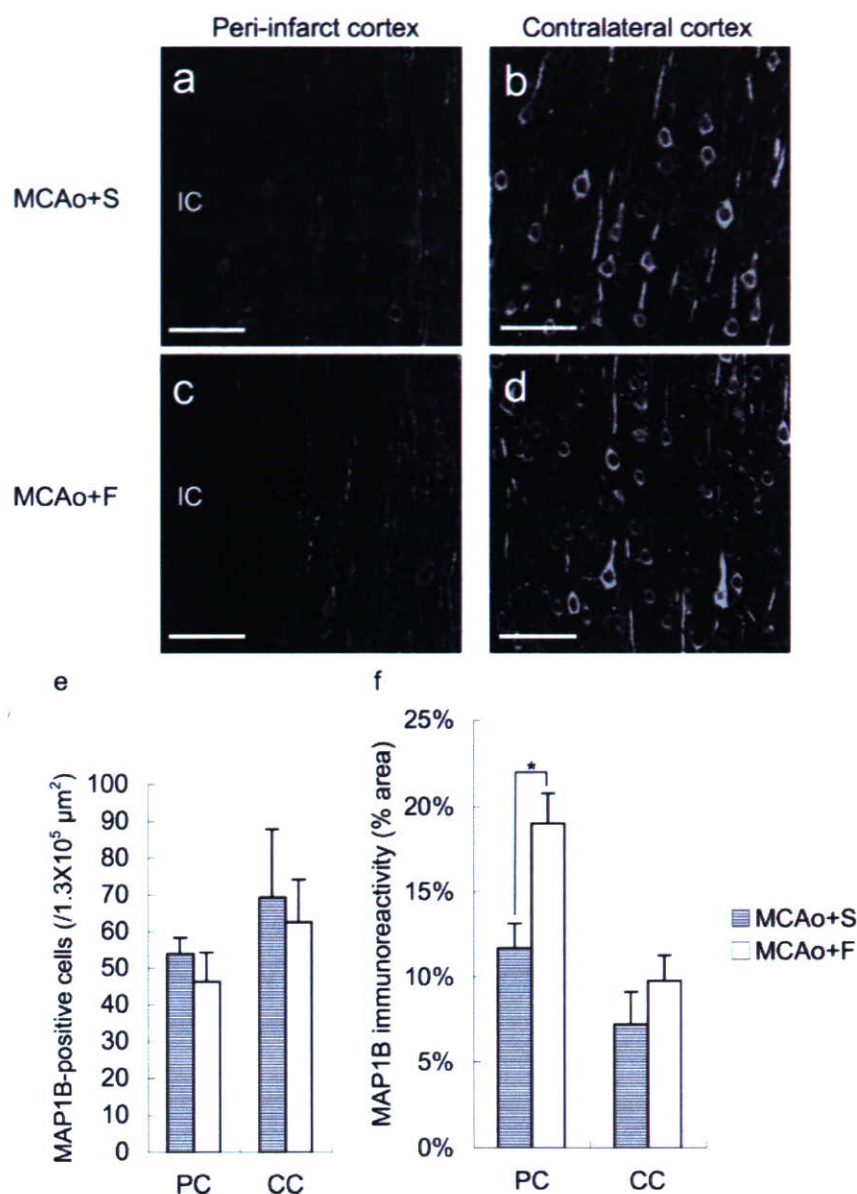
Figure 4. Typical images of immunohistochemical staining for MAP1B in peri-infarct cortex (a and c) and contralateral cortex (b and d) on day 14 (bar=100 μm). Although the number of MAP1B-positive cells was the same in both groups (e), immunoreactivity was higher in the peri-infarct region in fluvastatin-treated rats (f) (n=4 in each group, *$P<0.05$).

thalamic nuclei persisted as long as 9 months after focal cerebral ischemia.[12] Although immunohistochemical staining showed marked deposition of Aβ in the ventrolateral and ventromedial thalamic nuclei at 3 months after stroke, the area of Aβ deposits was significantly decreased in fluvastatin-treated rats (Figure 5f to 5h). In other regions, such as cortex or basal ganglia, there was no Aβ deposits in both groups as reported before.[12]

Discussion

Although several laboratories have shown that long-term pretreatment with a statin reduces infarct size in rodents,[19] no articles have reported the effects of delayed postischemic treatment with statins. The present study demonstrated that statin treatment beginning 7 days after ischemic stroke resulted in significant improvement of spatial learning at 8 weeks after stroke, without any change in the plasma cholesterol level and infarct size.

Fluvastatin-treated rats showed a significant increase of MAP1B in neurites in the peri-infarct region. Considering that MAP1B is especially prominent in extending neurites[20] and related to functional recovery after ischemic stroke,[17] one of the possible effects of fluvastatin is to enhance neurite outgrowth, "neuritogenesis," in the early stage of treatment. This speculation might be supported by the recent study demonstrating that neurite outgrowth is accelerated by pravastatin via inhibiting the activity of geranylgeranylated proteins such as RhoA.[21]

As BrdU/CD31-positive cells were increased 14 days after MCAo and microvessels were also increased in the peri-infarct region 100 days after MCAo, fluvastatin enhanced angiogenesis and resulted in improvement of microcirculation in the peri-infarct region. Although the relationship between the improved microcirculation and behavior is still unclear, a recent report demonstrated that the restoration of perfusion by collateral growth and new capillaries in the
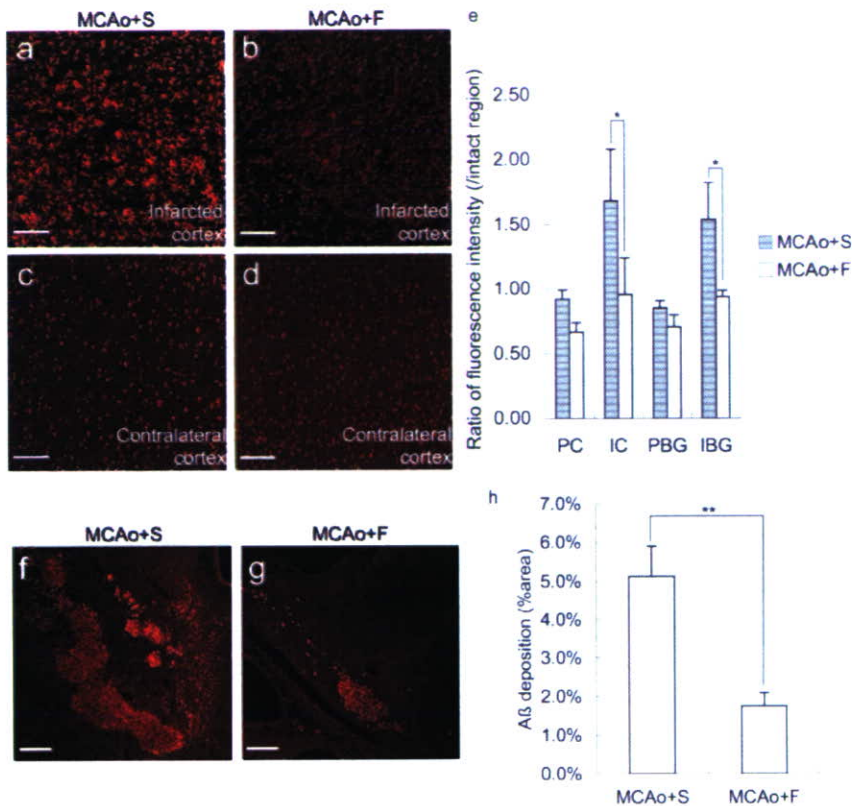
Figure 5. a through e, Superoxide anion detected by dihydroethidium staining on day 14. Red spots show the existence of superoxide anion. Fluorescence intensity was higher in the infarcted cortex (a) compared with the contralateral cortex (c). Fluvastatin-treated rats showed decreased fluorescence intensity in the infarcted cortex (b), although there was no difference in the peri-infarct cortex and basal ganglia (e) ($n=4$ in each group, $*P<0.05$, bar=100 μm). Deposition of Aβ in thalamus on day 100 after middle cerebral artery occlusion. Although deposition of Aβ was observed in the thalamic nuclei (f and g), there was no deposition in other regions such as the cortex and basal ganglia. Quantitative analysis showed decreased Aβ deposition in fluvastatin-treated rats (h) ($n=6$ in each group, $**P<0.01$, bar=200 μm).

ischemic border zone around a cortical infarct supported long-term functional recovery in rats.[22] Additionally, others reported that some patients who received tissue plasminogen activator therapy with no immediate clinical improvement despite early recanalization showed delayed clinical improvement.[23] From these viewpoints, it is likely that the improvement of microcirculation is an important factor for the functional recovery.

Of importance, fluvastatin reduced deposition of Aβ in the ventrolateral–ventromedial thalamic nuclei in the chronic stage of ischemic stroke, although rats subjected to focal cerebral ischemia develop deposition of Aβ in the ventroposterior lateral and ventroposterior medial nuclei for as long as 9 months.[12] This might be similar with precious reports showing that statins reduced the production of Aβ in Alzheimer disease.[24] The mechanism of the reduction of Aβ by fluvastatin should be further investigated.

Thus, the rats treated with fluvastatin showed enhancement of angiogenesis and neurite outgrowth in the peri-infarct cortex and reduced deposition of Aβ in the ventrolateral–ventromedial thalamic nuclei. Because those regions are important sites for spatial learning,[25,26] we speculate that the enhancement of functional recovery by fluvastatin might be dependent on those regions.

The other histological difference was the reduction of superoxide anion in the ischemic core in fluvastatin-treated rats. Because cerebral blood flow in the ischemic cortex remained to be reduced for 48 hours and restored to some extent 9 days after permanent MCAo,[27] we speculate that fluvastatin could reach the ischemic core and show the antioxidative effects. On the contrary, in the peri-infarct region, superoxide anion was not detected even in the control group and no effect of fluvastatin might be observed. This effect of statin is similar with the previous report showing that cerivastatin prevented the production of superoxide anion in the cerebral parenchyma in stroke-prone spontaneously hypertensive rats.[28] Also, fluvastatin is reported to possess antioxidative properties in other cells.[29,30]

The association of neurogenesis is also the center of interest, because previous reports showed an increase in neurogenesis after atorvastatin treatment beginning at 1 day after stroke.[5] However, we speculate that neurogenesis might not have contributed to the favorable outcome in the present study, because the volume of infarction was not decreased by fluvastatin, and the density of mature neurons (NeuN-positive cells) and proliferative immature neurons (BrdU/DCX-positive cells) was the same in both groups. From the viewpoints, the timing of treatment seems important for the enhancement of neurogenesis and the beginning of statin 7 days after MCAo might be too late to enhance neurogenesis.

The limitation of the present study is that there is no data demonstrating that fluvastatin crossed over the blood–brain barrier and acted on neurons directly. Blood–brain barrier permeability differs among statins and correlates in part with their respective lipophilicity.[31] Considering that pretreatment with pravastatin and rosuvastatin, whose lipophilicity is 0.84 and 0.33, respectively, shows significant effects on reducing infarction volume,[31] fluvastatin, whose lipophilicity is 1.27, might penetrate blood–brain barrier and have some direct effects on neurons. Otherwise, fluvastatin could penetrate the brain because of the disruption of blood–brain barrier after MCAo. One of other limitations in the present study is no

examination of the characteristics of BrdU positive-cells other than CD31, DCX, or NeuN. In addition, how these histological changes in fluvastatin-treated rats were mechanistically linked to improved outcome was not clarified. Further study is necessary to clarify these points.

Summary

Overall, delayed postischemic chronic fluvastatin treatment showed beneficial effects on the recovery of cognitive impairment after stroke by enhancement of neuritogenesis and of angiogenesis and a decrease in $A\beta$ deposition and superoxide anion production. Further studies might show potential clinical utility to treat cognitive impairment in patients with ischemic stroke.

Acknowledgments

Sources of Funding

Disclosures

Fluvastatin was donated from Novartis Pharma. Masataka Sata received Honoraria payment (modest) from Novartis Pharma. Ryuichi Morishita received honoraria payment (modest) and has an advisory board relationship to Novartis Pharma.

References

1. Sacks FM, Pfeffer MA, Moye LA, Rouleau JL, Rutherford JD, Cole TG, Brown L, Warnica JW, Arnold JM, Wun CC, Davis BR, Braunwald E. The effect of pravastatin on coronary events after myocardial infarction in patients with average cholesterol levels: cholesterol and recurrent events trial investigators. *N Engl J Med.* 1996;335:1001–1009.
2. Amarenco P, Tonkin AM. Statins for stroke prevention: disappointment and hope. *Circulation.* 2004;109:III44–49.
3. Moonis M, Kane K, Schwiderski U, Sandage BW, Fisher M. HMG-CoA reductase inhibitors improve acute ischemic stroke outcome. *Stroke.* 2005;36:1298–1300.
4. Chen J, Zhang C, Jiang H, Li Y, Zhang L, Robin A, Katakowski M, Lu M, Chopp M. Atorvastatin induction of VEGF and BDNF promotes brain plasticity after stroke in mice. *J Cereb Blood Flow Metab.* 2005;25:281–290.
5. Chen J, Zhang ZG, Li Y, Wang Y, Wang L, Jiang H, Zhang C, Lu M, Katakowski M, Feldkamp CS, Chopp M. Statins induce angiogenesis, neurogenesis, and synaptogenesis after stroke. *Ann Neurol.* 2003;53:743–751.
6. Zhang L, Zhang ZG, Ding GL, Jiang Q, Liu X, Meng H, Hozeska A, Zhang C, Li L, Morris D, Zhang RL, Lu M, Chopp M. Multitargeted effects of statin-enhanced thrombolytic therapy for stroke with recombinant human tissue-type plasminogen activator in the rat. *Circulation.* 2005;112:3486–3494.
7. Belayev L, Alonso OF, Busto R, Zhao W, Ginsberg MD. Middle cerebral artery occlusion in the rat by intraluminal suture: neurological and pathological evaluation of an improved model. *Stroke.* 1996;27:1616–1623.
8. Sata M, Nishimatsu H, Osuga J, Tanaka K, Ishizaka N, Ishibashi S, Hirata Y, Nagai R. Statins augment collateral growth in response to ischemia but they do not promote cancer and atherosclerosis. *Hypertension.* 2004;43:1214–1220.
9. Nakatomi H, Kuriu T, Okabe S, Yamamoto S, Hatano O, Kawahara N, Tamura A, Kirino T, Nakafuku M. Regeneration of hippocampal pyramidal neurons after ischemic brain injury by recruitment of endogenous neural progenitors. *Cell.* 2002;110:429–441.
10. Petullo D, Masonic K, Lincoln C, Wibberley L, Teliska M, Yao DL. Model development and behavioral assessment of focal cerebral ischemia in rats. *Life Sci.* 1999;64:1099–1108.
11. Cavaglia M, Dombrowski SM, Drazba J, Vasanji A, Bokesch PM, Janigro D. Regional variation in brain capillary density and vascular response to ischemia. *Brain Res.* 2001;910:81–93.
12. van Groen T, Puurunen K, Maki HM, Sivenius J, Jolkkonen J. Transformation of diffuse beta-amyloid precursor protein and beta-amyloid deposits to plaques in the thalamus after transient occlusion of the middle cerebral artery in rats. *Stroke.* 2005;36:1551–1556.
13. Iwai M, Liu HW, Chen R, Ide A, Okamoto S, Hata R, Sakanaka M, Shiuchi T, Horiuchi M. Possible inhibition of focal cerebral ischemia by angiotensin II type 2 receptor stimulation. *Circulation.* 2004;110:843–848.
14. Robinson RG. Differential behavioral and biochemical effects of right and left hemispheric cerebral infarction in the rat. *Science.* 1979;205:707–710.
15. DeVries AC, Nelson RJ, Traystman RJ, Hurn PD. Cognitive and behavioral assessment in experimental stroke research: Will it prove useful? *Neurosci Biobehav Rev.* 2001;25:325–342.
16. Badan I, Platt D, Kessler C, Popa-Wagner A. Temporal dynamics of degenerative and regenerative events associated with cerebral ischemia in aged rats. *Gerontology.* 2003;49:356–365.
17. Badan I, Dinca I, Buchhold B, Suofu Y, Walker L, Gratz M, Platt D, Kessler CH, Popa-Wagner A. Accelerated accumulation of n- and c-terminal beta app fragments and delayed recovery of microtubule-associated protein 1b expression following stroke in aged rats. *Eur J Neurosci.* 2004;19:2270–2280.
18. Schabitz WR, Berger C, Kollmar R, Seitz M, Tanay E, Kiessling M, Schwab S, Sommer C. Effect of brain-derived neurotrophic factor treatment and forced arm use on functional motor recovery after small cortical ischemia. *Stroke.* 2004;35:992–997.
19. Endres M, Laufs U, Liao JK, Moskowitz MA. Targeting enos for stroke protection. *Trends Neurosci.* 2004;27:283–289.
20. Gonzalez-Billault C, Avila J, Caceres A. Evidence for the role of map1b in axon formation. *Mol Biol Cell.* 2001;12:2087–2098.
21. Pooler AM, Xi SC, Wurtman RJ. The 3-hydroxy-3-methylglutaryl co-enzyme a reductase inhibitor pravastatin enhances neurite outgrowth in hippocampal neurons. *J Neurochem.* 2006;97:716–723.
22. Wei L, Erinjeri JP, Rovainen CM, Woolsey TA. Collateral growth and angiogenesis around cortical stroke. *Stroke.* 2001;32:2179–2184.
23. Alexandrov AV, Hall CE, Labiche LA, Wojner AW, Grotta JC. Ischemic stunning of the brain: Early recanalization without immediate clinical improvement in acute ischemic stroke. *Stroke.* 2004;35:449–452.
24. Fassbender K, Simons M, Bergmann C, Stroick M, Lutjohann D, Keller P, Runz H, Kuhl S, Bertsch T, von Bergmann K, Hennerici M, Beyreuther K, Hartmann T. Simvastatin strongly reduces levels of Alzheimer's disease beta-amyloid peptides Abeta 42 and Abeta 40 in vitro and in vivo. *Proc Natl Acad Sci U S A.* 2001;98:5856–5861.
25. Casu MA, Wong TP, De Koninck Y, Ribeiro-da-Silva A, Cuello AC. Aging causes a preferential loss of cholinergic innervation of characterized neocortical pyramidal neurons. *Cereb Cortex.* 2002;12:329–337.
26. Jeljeli M, Strazielle C, Caston J, Lalonde R. Effects of ventrolateral-ventromedial thalamic lesions on motor coordination and spatial orientation in rats. *Neurosci Res.* 2003;47:309–316.
27. Rudin M, Baumann D, Ekatodramis D, Stirnimann R, McAllister KH, Sauter A. MRI analysis of the changes in apparent water diffusion coefficient, t(2) relaxation time, and cerebral blood flow and volume in the temporal evolution of cerebral infarction following permanent middle cerebral artery occlusion in rats. *Exp Neurol.* 2001;169:56–63.
28. Kawashima S, Yamashita T, Miwa Y, Ozaki M, Namiki M, Hirase T, Inoue N, Hirata K, Yokoyama M. HMG-CoA reductase inhibitor has protective effects against stroke events in stroke-prone spontaneously hypertensive rats. *Stroke.* 2003;34:157–163.
29. Sumi D, Hayashi T, Thakur NK, Jayachandran M, Asai Y, Kano H, Matsui H, Iguchi A. A HMG-CoA reductase inhibitor possesses a potent anti-atherosclerotic effect other than serum lipid lowering effects–the relevance of endothelial nitric oxide synthase and superoxide anion scavenging action. *Atherosclerosis.* 2001;155:347–357.
30. Morita H, Saito Y, Ohashi N, Yoshikawa M, Katoh M, Ashida T, Kurihara H, Nakamura T, Kurabayashi M, Nagai R. Fluvastatin ameliorates the hyperhomocysteinemia-induced endothelial dysfunction: The antioxidative properties of fluvastatin. *Circ J.* 2005;69:475–480.
31. Endres M. Statins and stroke. *J Cereb Blood Flow Metab.* 2005;25:1093–1110.

Table I.   Statistics in Morris Water Maze

	Hidden Test			Visible Test		
	Latency	Length	Speed	Latency	Length	Speed
P values in 2-factor repeated-measure ANOVA (Sham, MCAo+S, MCAo+F)						
Treatment	<0.001	<0.001	0.053	0.004	0.021	0.342
Day	<0.001	0.011	<0.001	0.003	0.014	0.288
Treatment×Day	0.002	<0.001	0.855	0.465	0.684	0.306
P values in Scheffe test on day 4						
Sham vs MCAo+S	<0.001	<0.001	0.933	0.018	0.025	0.585
Sham vs MCAo+F	0.024	0.010	0.277	0.138	0.058	0.266
MCAo+S vs MCAo+F	0.012	0.023	0.129	0.643	0.941	0.820

MCAo+S indicates saline-treated rats after MCAo; MCAo+F, fluvastatin-treated rats after MCAo.